# Super-Antireflective Structure Films with Precisely Controlled Refractive Index Profile

*Kiwoon Choi, Youngwoon Yoon, Jaehoon Jung, Chi Won Ahn, Gil Ju Lee, Young Min Song, Min Jae Ko, Han Sup Lee, BongSoo Kim,* and Il-Suk Kang**

Light reflection occurs at the interface between media having different refractive indices and increases significantly as the angle of incidence (AOI) of light deviates from the normal direction.[1] AOI-dependent light reflection must be minimized for diverse optical applications, particularly building- and vehicle-integrated solar cells receiving oblique light for most of the day. In this regard, the development of antireflective (AR) films with a broadband, omnidirectional nature have been a critical issue.[2,3]

It is well known that graded refractive index (GRIN) layers can effectively reduce surface reflection through optical impedance matching with a gradual transition in the refractive index (RI, $n$) from air to the substrate.[2,3] Two categories of conventional approaches for the fabrication of GRIN layers have been reported. One is to prepare multi-sublayer coatings with different RIs in each layer.[4–7] Conceptually, as the number of sublayers increases, the RI difference between the $i$th and ($i$ + 1)th sublayers ($\Delta n$) becomes very small and thus, the AR properties of the multi-sublayer coatings improve.[8] However, to date, the lowest known RI value of a dense material is ≈1.4, which is still far higher than the RI of air. Accordingly, porous structures have been considered. Using an oblique-angle deposition method, $SiO_2$ nanorod based GRIN films with RI values as low as 1.05 have been prepared.[5] However, the fabrication of $SiO_2$ nanorod sublayers inclined at several angles with oblique-angle deposition requires very delicate control. Moreover, such stacked structures of inclined nanorod layers are mechanically unstable. As a result, the number of sublayers and the GRIN layer thickness must be limited, which means that there will be abrupt RI changes between the sublayers and thus, the AR properties will diminish, especially at high AOIs. An alternative approach is to prepare a continuously tapered subwavelength structure on the surface, as inspired by the corneal nipple arrays of moth eyes.[9–16] By carving biomimetic silicon nanotips on the surface, a GRIN layer with a quasilinear profile and a thickness of 1.6 μm has recently been prepared.[9] However, such nanotip GRIN layers are not mechanically stable, so the GRIN layer thickness cannot be further increased, which leads to a limited improvement in AR properties. Recently, polymer-based flexible AR films have been demonstrated, but they are neither weather-resistant nor robust. Despite these efforts in developing many AR films, the current state-of-the-art AR properties of films still need to be improved, especially for high AOIs.[4–7,9–16] New breakthrough technology is therefore required to push the limit of broadband and omnidirectional AR properties to the theoretically achievable level and to retain the initial AR properties after aging.

In this contribution, we report the fabrication of super-antireflective structure (S-ARS) films that exhibit an unprecedented RI profile and eliminate reflections almost completely for any AOI. Moreover, they are mechanically robust and self-cleaning. We first conducted optical simulations in searching for an ideal RI profile of a GRIN layer based on an aluminum foil and realized an optically modeled AR nanostructure with extreme precision using a newly developed square voltage pulse anodization (SPA) method. The application of our S-ARS films on polymer solar cells (PSCs) demonstrated that the power conversion efficiencies (PCEs) of the PSC with the S-ARS film increased to 12.08% at an AOI of 70° and the PCE improvements reached 93.3% at an AOI of 85°.

To design the broadband, omnidirectional AR films, we began with optical modeling on a GRIN layer. The absolute reflectance of the GRIN layer depends on its RI profile and thickness. The modified quantic (M-Q) profile was adopted for optical modeling, which has exhibited the best AR property among exponential sine, cubic, and quintic profiles.[8,17–19] **Figure 1**a shows the M-Q profile with RI matching between air ($n$ = 1.00) and a substrate ($n$ = 1.77) used in our theoretical

Dr. K. Choi, J. Jung, Dr. C. W. Ahn, Dr. I.-S. Kang
National Nanofab Center
Korea Advanced Institute of Science and Technology
291, Daehak-ro, Yuseong-gu
Daejeon 34141, Republic of Korea
E-mail: arock76@naver.com
Dr. Y. Yoon, Dr. M. J. Ko
Photoelectronic Hybrids Research Center
Korea Institute of Science and Technology (KIST)
5, Hwarang-ro 14-gil, Seongbuk-gu
Seoul 02792, Republic of Korea
G. J. Lee, Prof. Y. M. Song
School of Electrical Engineering and Computer Science
Gwangju Institute of Science and Technology
123 Cheomdan-gwagiro, Buk-gu
Gwangju 61005, Republic of Korea
Dr. M. J. Ko
Green School and KU-KIST Graduate School of
Converging Science and Technology
Korea University
145, Anam-ro, Seongbuk-gu, Seoul 02841, Republic of Korea
Prof. H. S. Lee
Department of Advanced Fiber Engineering
Inha University
100, Inha-ro, Nam-gu, Incheon 22212, Republic of Korea
Prof. B. Kim
Department of Science Education
Ewha Womans University
52, Ewhayeodae-gil, Seodaemun-gu
Seoul 03760, Republic of Korea
E-mail: bongsoo@ewha.ac.kr

**DOI: 10.1002/adom.201600616**

  

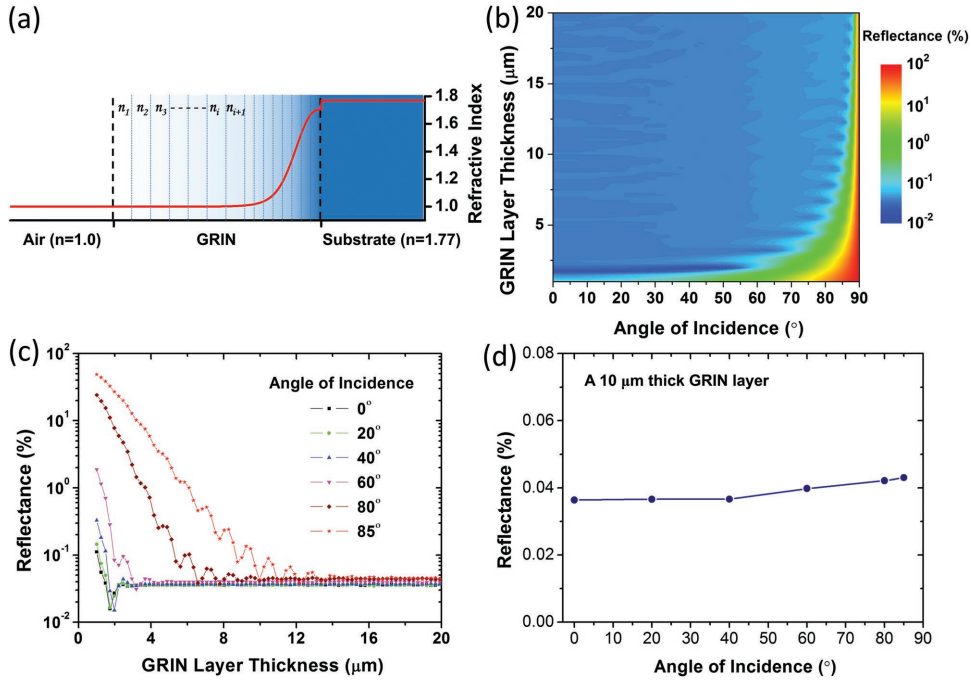


**Figure 1.** Optical simulation for an ideal GRIN layer. a) M–Q profile with RI matching between air and a substrate with $n = 1.77$. b) Calculated angular-dependent reflectance of 633 nm wavelength light incident on a surface with the M-Q profile for GRIN layer thicknesses up to 20 μm. c) Calculated reflectance for various AOIs from 0° to 85° as a function of the thickness. d) Calculated reflectance of 10 μm thick GRIN layer from 0° to 85°.

reflectance calculations. The calculated AOI-dependent reflectance of light ($\lambda = 633$ nm) is shown in Figure 1b as a function of GRIN layer thicknesses up to 20 μm. The surface reflection increases with the AOI and decreases with GRIN layer thickness, consistent with previous reports.[2,8] The calculated reflectance values for AOIs from 0° to 85° were replotted as a function of the GRIN layer thickness in Figure 1c. For normal incidence (0°), a reflectance of ≈0.1% was observed for a thickness of 1 μm and the reflectance reached its limit (≈0.036%) rapidly as the GRIN layer thickness increased. For an extreme AOI of 85°, a high reflectance of ≈50% was observed for a thickness of 1 μm and the reflectance decreased much more slowly as the thickness increased. Note that a GRIN layer thicker than 10 μm revealed very weak AOI dependence (Figure 1d). Thus, to ensure super omnidirectional AR properties, the GRIN layer should be thicker than 10 μm.

In formation of the modeled 10 μm GRIN layer, a hexagonal pore nanostructure would be suitable to provide a material with minimal density as well as high mechanical stability, because a mechanical stress applied to any point of this structure is redistributed to the walls of neighboring pores.[10,20] As long as the pore period is sufficiently small with respect to the wavelength of the incident light, the effective RI ($n_{\text{eff}}$) at any height ($z$) in the hexagonal pore structure can be calculated approximately with the equation $n_{\text{eff}}(z) = \{f_{\text{bulk}}(z) \cdot n_{\text{bulk}}^{2/3} + (1 - f_{\text{bulk}}(z)) \cdot n_{\text{air}}^{2/3}\}^{3/2}$.[1,2,19] Here, $n_{\text{bulk}}$ and $n_{\text{air}}$ are the RI values of the bulk material and air, respectively, and $f_{\text{bulk}}(z)$ is the bulk material fraction at height $z$. $f_{\text{bulk}}(z)$ for the hexagonal pore structure is given by $f_{\text{bulk}}(z) = 1 - \pi D(z)^2/2\sqrt{3}d^2$, where $D(z)$ is the pore diameter at height $z$ and $d$ is the pore period. Finally, $n_{\text{eff}}(z)$ is a function of $D(z)$, which means that the RI profile can be finely tuned by precisely controlling the pore profile in the $z$ direction.

Additionally, the anodization of aluminum is a perfect method for the fabrication of thick nanostructures with hexagonal pores.[21–23] Delicate maneuvers in control of the electrochemical treatment conditions have great potential in the preparation of anodized aluminum oxide (AAO) nanopores with the desired depths and diameters.[24] For these reasons, we developed a facile technique of SPA enabling a robust hexagonal pore structure with a theoretically predicted ideal RI profile up to extremely low RI values.

**Figure 2**a,b illustrates how the SPA method generates sublayers of tapered nanopores with various diameters and depths. Unlike conventional anodizing processes, which are generally performed at 0 °C,[22,23] the SPA process in this study was performed at 35 °C. At this temperature, the anodizing electrolytes etch the AAO significantly, whereas etching is almost completely suppressed at 0 °C. Thus, in the SPA process, lateral pore widening occurs throughout the process during the cycle period ($T$), whereas vertical pore drilling takes place only during the application of the square voltage–pulse-on ($t$). The $n$-cycle SPA process can produce pores consisting of $n$ sublayers, as follows. In the first SPA cycle, pore drilling is initiated. The pore depth and the initial pore diameter in the first sublayer are determined by the voltage-on time ($t_1$) and the period ($T_1$) of the first cycle, respectively (Equations (S5) and (S6), Supporting Information). During the second cycle, a second sublayer is created below the first sublayer. The pore depth and the initial pore diameter in the second sublayer are also determined by the voltage-on time ($t_2$) and the period ($T_2$) of the second cycle, respectively. During $T_2$, the pores in the first sublayer are simultaneously widened as well. After repeating the SPA cycle $n$ times (the $n$th cycle), pores consisting of $n$ sublayers with various depths and diameters form, as shown in Figure 2b.

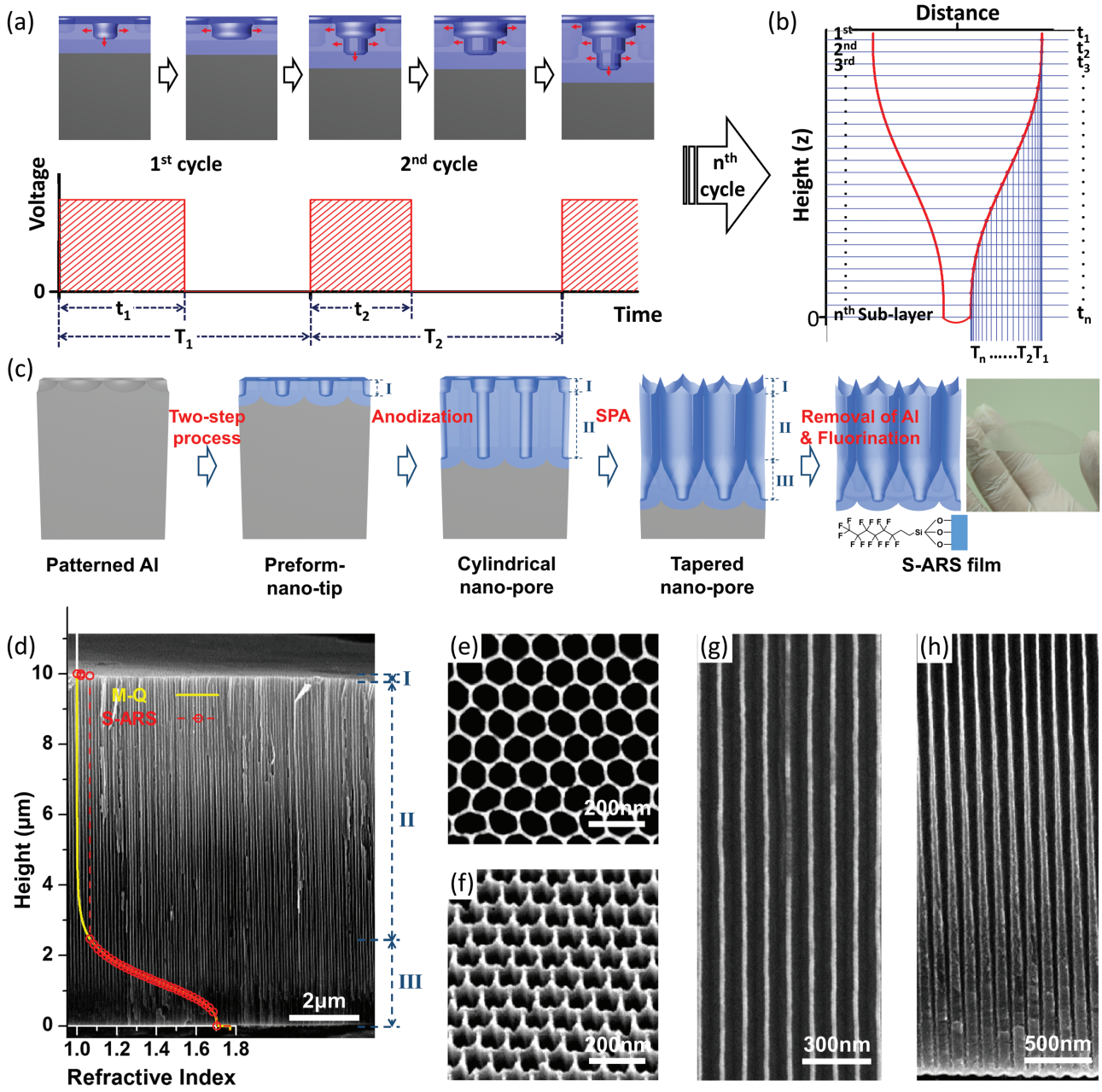


**Figure 2.** Fabrication of the S-ARS film with the SPA method. a) Schematic diagram of the SPA method for the fabrication of sublayers with different diameters and depths. b) Schematic diagram of a pore profile consisting of *n* sublayers after the *n*th SPA cycle. c) Schematic diagram of the fabrication process of the S-ARS film and photograph of the resulting S-ARS film. d) Cross-sectional SEM image of the S-ARS film. The M-Q profile (solid yellow line) and the RI profile of the S-ARS film (dashed red line and open-circles) are overlaid on the image. e) Top view of the S-ARS film. f) Oblique view showing the nanotips in Region I. g) Cross-sectional view showing the cylindrical nanopores in Region II. h) Cross-sectional view showing the tapered nanopores in Region III.

Here, the pore depth ($L_i$) in the $i$th sublayer is determined by the corresponding voltage-on time ($t_i$). The height ($z_i$) of the $i$th sublayer from the pore bottom is determined by the accumulated voltage-on time from $t_i$ to $t_n$ $\left(\sum_i^n t_i\right)$, and the overall pore depth is determined by the total voltage-on time $\left(\sum_1^n t_i\right)$. The pore diameter ($D_i$) in the $i$th sublayer is determined by the accumulated periods from $T_i$ to $T_n$ $\left(\sum_i^n T_i\right)$, and $D_1$ is determined by the total period $\left(\sum_1^n T_i\right)$. This whole process can be programed to produce the desired number of sublayers and the desired $D_i$. Thus, this SPA method enables the preparation of a material with a virtually continuous RI transition, in excellent accordance with the M-Q profile, with extreme precision.

A 10 µm thick GRIN layer having an almost ideal M-Q profile was realized by the combinational application of the conventional anodization and the SPA method on alumina substrates. Its profile is composed of three major regions: a first short region to reproduce the RI of air (50 nm thickness, Region I), a long constant region with RI = 1.065 (7.48 µm thickness, Region II), and a transition region with RI values from 1.065 to 1.704 (2.47 µm thickness, Region III). Each region was prepared as followed: nanotip ($D(z) > d$, Region I) using a two-step process consisting of a conventional anodization at 0 °C and an etching at 35 °C, cylindrical nanopore ($D(z) \approx d$, Region II) by using a conventional anodization at 0 °C, and tapered nanopore ($D(z) < d$, Region III) using the SPA method at 35 °C. The desired pore diameters were completed after the SPA process. To ensure the persistence of the manufactured AR films for a long period under weather conditions,[10–13] a surface fluorination was carried out.[25] Finally, the remaining Al substrate was removed, resulting in a free-standing film as shown in the photograph of Figure 2c. This fluorinated and nanotip-structured AR film exhibits superhydrophobic, i.e., self-cleaning properties with a contact angle of 154° (Figure S1, Supporting Information). The experimental processes used are shown schematically in Figure 2c (for more detailed processes, see the Supporting Information).

The fabricated pore profiles were confirmed by obtaining scanning electron microscopy (SEM) images of the resulting AR film (Figure 2d–h). The M-Q profile of an ideal 10 µm thick GRIN layer based on alumina substrates maintains virtually the RI value of air up to a depth of 7.53 µm and then RI increases rapidly to a value close to that of dense alumina, as indicated by the solid yellow line overlaid in Figure 2d. Because the minimum RI that can be developed while maintaining a flat surfaced AAO structure with hexagonal pore lattice for mechanical stability is 1.065,[23] the practical RI profile for the S-ARS was modified slightly from that of the M-Q profile, as indicated by the dashed red line and open circles overlaid in Figure 2d. The AR film is 10 µm thick (Figure 2d) and its surface is composed of pores in a hexagonal lattice of 105 nm (Figure 2e),[23] which is small enough to prevent any significant Mie and Rayleigh scattering of visible light.[18,26] Figure 2f–h presents the pore profiles corresponding to the three regions; the nanotips in Region I (Figure 2f) and the cylindrical nanopores in Region II (Figure 2g) were well fabricated, and the pore profile in Region III is ideally tapered without any abrupt steps (Figure 2h).

The transmittance of our transparent stand-alone AR film was measured at various AOIs with an aperture setup (**Figure 3**a). Incident light passing through the AR film meets two surfaces, the nanostructured surface on the front of the film and the flat surface on the back; reflection occurs at both surfaces.[26] Figure 3b shows the wavelength-dependent specular transmittance of the AR film over the wavelength range 400–800 nm for AOIs of 0°, 40°, and 80°. The measured optical properties for all three angles are in good agreement with the M-Q profile-based theoretical calculations for the wavelength range 500–800 nm. The transmittances at wavelengths below 500 nm are slightly lower than the theoretical values, which is possibly due to light absorbing impurities trapped inside the AR film.[27] Figure 3c shows the angular-dependent specular transmittances

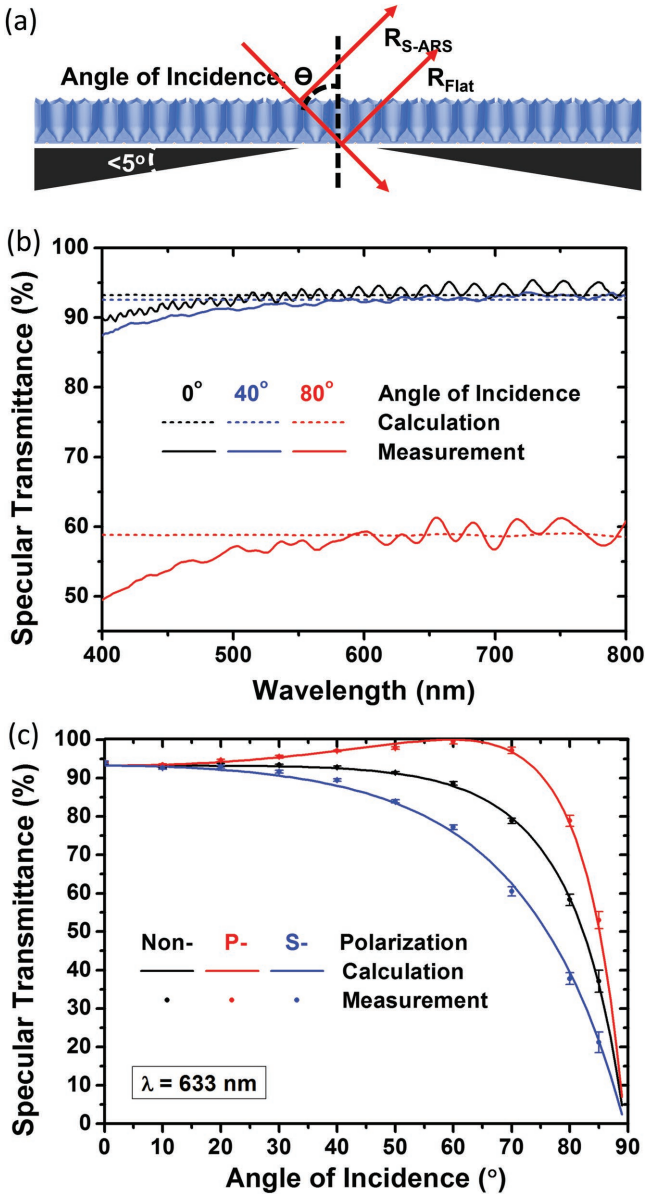


**Figure 3.** Optical characteristics of the S-ARS film. a) Schematic diagram of specular transmittance measurements obtained by using an aperture with a slope of <5° and a hole with a diameter of 10 mm. b) Calculated (M–Q profile) and measured (S-ARS film) wavelength-dependent specular transmittances over the wavelength range 400–800 nm for AOIs of 0°, 40°, and 80°. c) Calculated (M-Q profile) and measured (S-ARS film) angular-dependent specular transmittances for non-, *p*-, and *s*-polarized light with a wavelength of 633 nm.

for non-, *p*-, and *s*-polarized light with a wavelength of 633 nm. The measured data are also in good agreement with the M-Q profile-based theoretical calculations. These results indicate that the intended RI profile of the AR film has been prepared successfully and that the AR film has super broadband and omnidirectional properties. The specular transmittances, even at AOIs above 60°, were well-maintained and unprecedentedly higher than any reported values.[5,9,28,29] On the other hand, it was impossible to determine experimentally the exact value

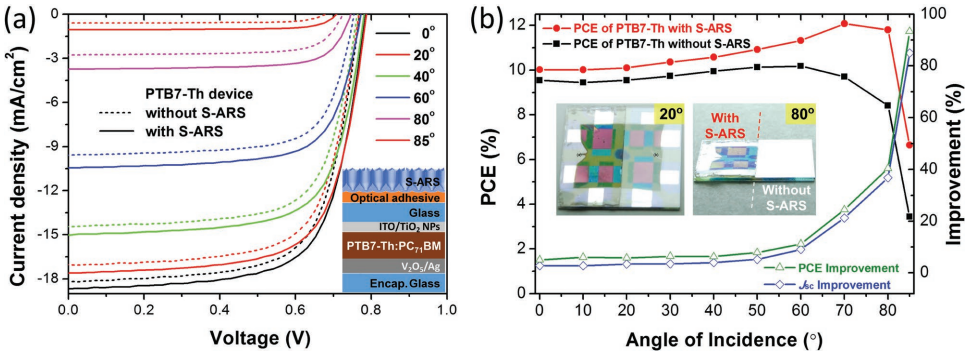


**Figure 4.** Device characteristics of a PSC incorporating the S-ARS film. a) *J–V* characteristics for PSC with and without the S-ARS film at AOIs between 0° and 80°. The inset shows a schematic diagram of the PSC device structure with the S-ARS film. b) Corresponding AOI-dependent PCE values of PSC with (red) and without (black) the S-ARS film, together with the AOI-dependent relative improvement in the $J_{sc}$ (blue) and PCE (green). The inset in (b) shows photographs of the PSC with (left-side) and without (right-side) the S-ARS film for AOIs of 20° and 80°, demonstrating that our S-ARS film has super omnidirectional AR properties. There are reflections from the bottom encapsulation glass in the peripheral area without the PTB7-Th:$PC_{71}BM$ layer.

of the reflectance only for the top surface of the S-ARS film ($R_{S\text{-}ARS}$) because of internal interference and reflection on the back of the S-ARS film ($R_{Flat}$).[26] However, the excellent agreement between our measurements and calculations means that the experimental $R_{S\text{-}ARS}$ values can be estimated from the corresponding calculated values in Figure 1b: i.e., 0.036% and 0.043% at 0° and 85°, respectively.

The transparent stand-alone S-ARS film can be applied in many substrates and can be beneficial for diverse optical devices such as solar cells,[11,12,15,16] because nanostructures directly integrated on the cell surface could lead to severe surface recombination, which degrades the cell performance, or require complex and time consuming fabrication schemes.[18,19] To demonstrate this, we investigated the photovoltaic properties of PSCs based on the photoactive layer of a PTB7-Th:$PC_{71}BM$ (Poly(2-ethylhexyl 4-(4,8-bis((2-ethylhexyl)oxy)benzo[1,2-b:4,5-b′] dithiophen-2-yl)-3-fluorothieno[3,4-b]thiophene-2-carboxylate, PTB7; Poly(2-ethylhexyl 4-(4,8-bis(5-(2-ethylhexyl)thiophen-2-yl) benzo[1,2-b:4,5-b′]dithiophen-2-yl)-3-fluorothieno[3,4-b]thiophene-2-carboxylate), PTV7-Th; [6,6]-phenyl-C71-butyric acid methyl ester, $PC_{71}BM$) blend[30] with and without the S-ARS film. **Figure 4**a shows the current density–voltage (*J–V*) curves at various AOIs between 0° and 85° and the device structure of S-ARS/glass/indium tin oxide (ITO)/$TiO_2$ nanoparticles/photoactive/$V_2O_5$/Ag. Figure 4b compares the corresponding AOI-dependent PCEs and improvements in $J_{sc}$ and PCE of the PSC with and without the S-ARS film. At the normal incidence of sunlight, the PCE of the PSC without the S-ARS film was observed to be 9.54%, with an open-circuit voltage ($V_{oc}$) of 0.77 V, a short-circuit current ($J_{sc}$) of 18.2 mA $cm^{-2}$, and a fill factor of 68% (we certified the photovoltaic properties of our cell at the Korea Institute of Energy Research, as shown in Figure S3 in the Supporting Information). After attaching the S-ARS film to this same device, it exhibited a significantly improved PCE of 10.02%, which corresponds to 5.03% PCE improvement. The increased external quantum efficiency (EQE) values in the range 400–800 nm (Figure S2, Supporting Information) confirmed that the S-ARS film effectively assisted light absorption in the PSC.

These improvements because of the S-ARS film occurred consistently and were more pronounced with high AOI illumination. Considering the light input power ($P_{in}$) change with AOI (see Figure S4, Supporting Information), the PCEs of the PSC with the S-ARS film increased to 12.08% at an AOI of 70° and the PCE improvements reached 93.3% at an AOI of 85°. All the results demonstrate that the S-ARS film prepared in this study indeed has super omnidirectional AR properties (the inset of Figure 4b shows photographs of the PSC with and without the S-ARS film for AOIs of 20° and 80°).

In conclusion, we have developed a novel SPA method for the ideal control of the RI profile far beyond the limit of conventional GRIN layers and successfully fabricated an unprecedented 10 μm thick S-ARS film with an RI profile mimicking the M-Q profile almost completely. The resulting S-ARS film was demonstrated to have super broadband and omnidirectional AR properties, up to 85°. The use of our transparent stand-alone S-ARS film in the PSC device was found to raise its PCE significantly, especially for high AOIs. Overall, we demonstrated that the S-ARS film fabricated by a facile SPA method is well-suited for solar cell applications. Furthermore, these films will be potentially applicable for devising optical components for diverse optical applications.[31]

## Experimental Section

*Optical Simulation*: Reflectance/transmittance spectra of alumina film with the M–Q RI profile were calculated by using the rigorous coupled-wave analysis (DiffractMod, RSoft Design Group, USA).[32] Three thousand index steps for graded layers and ninth diffraction order were used to calculate the diffraction efficiency, which was a sufficient number to stabilize the results numerically. The RI value ($n$ = 1.77) for the alumina was taken from the literature.[33] Dispersion/absorption was not considered in this calculation. The M-Q profile was taken from the equation represented in the ref. [8]. The nonpolarized light transmission, $T_{non}$ was determined by $T_{non} = (T_p + T_s)/2$, where $T_p$ and $T_s$ are the transmittance for the *p* and *s* linear polarizations, respectively.

*Optical Measurements*: S-ARS films with a diameter of 45 mm were prepared. An aperture having a slope of <5° and a hole of 10 mm in diameter was lab-produced and was located at the sample holder of directional reflectance/transmittance accessory in spectrophotometer (Perkin Elmer, lambda 650). These samples were mounted on the aperture and then the specular transmittance was measured at the slit width of 5 nm and the slit interval of 2 nm.

*Solar Cell Characteristics: J–V* characteristics were obtained on a Keithley model 2400 source measuring unit. A class-A solar simulator with a 150 W Xenon lamp (Yamashita Denso Corp.) was used as a light source. Its light intensity was set to AM 1.5 G 1 sun light intensity (100 mW $cm^{-2}$) by using a NREL-calibrated silicon photodiode G425 with a KG-5 filter. A home-made tilting accessory was used to measure the dependence of the angle of light incidence on the photovoltaic properties. Immediately after measuring the photovoltaic properties of PSCs, 10 mm diameter S-ARS films were attached on the glass side ($n$ = 1.52) of the PSCs using an optical adhesive (Norland, NOA164, $n$ = 1.64). The optical adhesive was hardened through a UV exposure of 20 s (8 W) and finally the coating of the S-ARS films was completed. To investigate the effect of the curing UV exposure or device degradation during solar cell property measurements on the photovoltaic properties, the photovoltaic properties were measured before coating the S-ARS films and after removing the coated S-ARS films. Identical photovoltaic properties of the PSCs ensured that all the photovoltaic performance differences between with and without S-ARS films could be solely attributed to the effect of the S-ARS films.

## Supporting Information

Supporting Information is available from the Wiley Online Library or from the author.

## Acknowledgements

This work was supported by a grant (2011-0032147) from the Center for Advanced Soft Electronics under the Global Frontier Research Program, a grant (NRF-2015M1A2A2056218) from the Technology Development Program to Solve Climate Changes of the National Research Foundation (NRF) funded by the Ministry of Science, ICT & Future Planning, a grant (NRF-2013R1A1A2011992) from the Basic Science Program through the NRF funded by the Ministry of Education, and a grant from the Open Innovation Lab Project from the National Nanofab Center (NNFC), Korea.

Received: July 27, 2016
Revised: September 27, 2016
Published online: November 7, 2016

[1] Y. Kanamori, M. Sasaki, K. Hane, *Opt. Lett.* **1999**, *24*, 1422.
[2] S. Chattopadhyay, Y. F. Huang, Y. J. Jen, A. Ganguly, K. H. Chen, L. C. Chen, *Mater. Sci. Eng., R* **2010**, *69*, 1.
[3] H. K. Raut, V. A. Ganesh, A. S. Nair, S. Ramakrishna, *Energy Environ. Sci.* **2011**, *4*, 3779.
[4] S. Chhajed, M. F. Schubert, J. K. Kim, E. F. Schubert, *Appl. Phys. Lett.* **2008**, *93*, 251108.
[5] J.-Q. Xi, M. F. Schubert, J. K. Kim, E. F. Schubert, M. Chen, S.-Y. Lin, W. Liu, J. A. Smart, *Nat. Photonics* **2007**, *1*, 176.
[6] S. R. Kennedy, M. J. Brett, *Appl. Opt.* **2003**, *42*, 4573.
[7] J. A. Hiller, J. D. Mendelsohn, M. F. Rubner, *Nat. Mater.* **2002**, *1*, 59.
[8] D. Poitras, J. Dobrowolski, *Appl. Opt.* **2004**, *43*, 1286.
[9] Y.-F. Huang, S. Chattopadhyay, Y.-J. Jen, C.-Y. Peng, T.-A. Liu, Y.-K. Hsu, C.-L. Pan, H.-C. Lo, C.-H. Hsu, Y.-H. Chang, C.-S. Lee, K.-H. Chen, L.-C. Chen, *Nat. Nanotechnol.* **2007**, *2*, 770.
[10] J.-G. Kim, H. J. Choi, K.-C. Park, R. E. Cohen, G. H. McKinley, G. Barbastathis, *Small* **2014**, *10*, 2487.
[11] K.-H. Tsui, Q. Lin, H. Chou, Q. Zhang, H. Fu, P. Qi, Z. Fan, *Adv. Mater.* **2014**, *26*, 2805.
[12] S. Y. Heo, J. K. Koh, G. Kang, S. H. Ahn, W. S. Chi, K. Kim, J. H. Kim, *Adv. Energy Mater.* **2014**, *4*, 1300632.
[13] J. van de Groep, P. Spinelli, A. Polman, *Nano Lett.* **2015**, *15*, 4223.
[14] A. Rahman, A. Ashraf, H. Xin, X. Tong, P. Sutter, M. D. Eisaman, C. T. Black, *Nat. Commun.* **2015**, *6*, 5963.
[15] J.-D. Chen, C. Cui, Y.-Q. Li, L. Zhou, Q.-D. Ou, C. Li, Y. Li, J.-X. Tang, *Adv. Mater.* **2015**, *27*, 1035.
[16] S.-F. Leung, K.-H. Tsui, Q. Lin, H. Huang, L. Lu, J.-M. Shieh, C.-H. Shen, C.-H. Hsu, Q. Zhang, D. Li, Z. Fan, *Energy Environ. Sci.* **2014**, *7*, 3611.
[17] B. Sheldon, J. Haggerty, A. Emslie, *J. Opt. Soc. Am. A* **1982**, *72*, 1049.
[18] W. H. Southwell, *J. Opt. Soc. Am. A* **1991**, *8*, 549.
[19] D. G. Stavenga, S. Foletti, G. Palasantzas, K. Arikawa, *Proc. R. Soc. Edinburgh, Sect. B: Biol. Sci.* **2006**, *273*, 661.
[20] R. Lakes, *Nature* **1993**, *361*, 511.
[21] W. Lee, S.-J. Park, *Chem. Rev.* **2014**, *114*, 7487.
[22] H. Masuda, K. Fukuda, *Science* **1995**, *268*, 1466.
[23] K. Nielsch, J. Choi, K. Schwirn, R. B. Wehrspohn, U. Gösele, *Nano Lett.* **2002**, *2*, 677.
[24] K. Choi, S. H. Park, Y. M. Song, Y. T. Lee, C. K. Hwangbo, H. Yang, H. S. Lee, *Adv. Mater.* **2010**, *22*, 3713.
[25] Y.-F. Chen, Y.-H. Hu, Y.-I. Chou, S.-M. Lai, C.-C. Wang, *Sens. Actuators, B: Chem.* **2010**, *145*, 575.
[26] Y. M. Song, H. J. Choi, J. S. Yu, Y. T. Lee, *Opt. Express* **2010**, *18*, 13063.
[27] J. Wang, C.-W. Wang, S.-Y. Li, F. Zhou, *Appl. Phys. A* **2009**, *94*, 939.
[28] J. W. Leem, S. Kim, S. H. Lee, J. A. Rogers, E. Kim, J. S. Yu, *Adv. Energy Mater.* **2014**, *4*, 1301315.
[29] D. Liang, Y. Huo, Y. Kang, K. X. Wang, A. Gu, M. Tan, Z. Yu, S. Li, J. Jia, X. Bao, S. Wang, Y. Yao, H. S. P. Wong, S. Fan, Y. Cui, J. S. Harris, *Adv. Energy Mater.* **2012**, *2*, 1254.
[30] S.-H. Liao, H.-J. Jhuo, Y.-S. Cheng, S.-A. Chen, *Adv. Mater.* **2013**, *25*, 4766.
[31] H. Kikuta, H. Toyota, W. Yu, *Opt. Rev.* **2003**, *10*, 63.
[32] M. Moharam, T. Gaylord, *J. Opt. Soc. Am. A* **1981**, *71*, 811.
[33] E. D. Palik, *Handbook of Optical Constants of Solids II*, Academic Press, NY, USA **1997**.